This article has been accepted for publication in a future issue of this journal, but has not been fully edited. Content may change prior to final publication. Citation information: DOI 10.1109/JSTQE.2019.2911420, IEEE Journal of Selected Topics in Quantum Electronics

Indium Phosphide Photonic Integrated Circuit Transceiver for FMCW LiDAR

Brandon J. Isaac, Bowen Song, Sergio Pinna, Larry A. Coldren, *Life Fellow, IEEE*, Jonathan Klamkin, *Senior Member, IEEE*

***Abstract*— We present a photonic integrated circuit (PIC) transceiver for frequency modulated continuous wave (FMCW) LiDAR applications. The transmitter consists of a widely tunable sampled grating distributed Bragg reflector laser (SGDBR) and a frequency discriminator which combines multimode interference couplers, a tunable asymmetric Mach-Zehnder Interferometer (a-MZI), and balanced photodiodes. The frequency discriminator converts frequency fluctuations of the laser to amplitude fluctuations of the photodiode currents. This provides an error signal for feedback into the laser cavity for frequency stabilization. Frequency modulation is obtained by a phase shifter in the a-MZI which tunes the quadrature point of the filter and the frequency where the error is zero. An on-chip receiver couples power from the transmitter to self-heterodyne with the time-delayed echo of a distance object. The generated beat frequency of the self-heterodyne measurement gives the echo signals time-of-flight to obtain the distance and velocity of the reflecting object. The theory of the components is described, and characterization of the transmitter and receiver are presented.**

***Index Terms*—LiDAR, Semiconductor Lasers, Photonics Integrated Circuits**

I. Introduction

TUNABLE lasers and photonic integrated circuits (PIC) have demonstrated performance improvements for several decades in the telecommunication industry enabling over 100 Gbps data rates [1-7]. Furthermore, advancements in silicon photonics have increasingly enabled integrated photonic platforms with high component density [4,6,7]. Beyond communication application, tunable lasers and PICs are enabling compact solutions for remote sensing, detection, and spectroscopy. Each individual application puts forth specific requirements on the PIC. Laser performance such as power output, linewidth, and tuning range become important parameters to optimize for the specific application. One emerging technology that can benefit from tunable lasers and photonic integration is Light Detection and Ranging, or LiDAR. In contrast to RaDAR, LiDAR utilizes signals at optical frequencies which improves the spatial resolution of the imaging, opening possible solutions to autonomous driving, robotics, and terrain mapping. There are several approaches to LiDAR as discussed in refs. [8-10]. Photonic integration opens the possibility to reduce the system size, as a single chip can contain many of the necessary system elements such as acting as both a tunable light source and receiver.

Compared to standard pulsed techniques for LiDAR, frequency modulated continuous wave (FMCW) LiDAR has the benefit of low peak power, which makes it a good candidate to implement in semiconductor waveguides [11-14]. In this approach, the laser frequency is modulated with a triangular waveform, and split to serve as both an output signal to an optical phased array (OPA) and a reference for the detection. The OPA can provide 2D beam steering by utilizing phase shifters for steering along one direction, and frequency dispersion of the optical antenna for steering along the orthogonal direction [15-17]. The reflected echo signal couples back through the OPA to a receiver where it is mixed with the reference signal to generate the measurement result. The frequency modulation allows the time-of-flight to be determined by the beat frequency generated in the receiver. The echo signal frequency is offset from the reference by $\delta f = 2\cdot(\Delta F/T)\cdot\delta t$, where ΔF is the total frequency modulation range, T is the period of the frequency modulation, and δt is the time-of-flight for the echo signal. The object distance can then be determined from $d = c\cdot(\delta t/2)$, where c is the speed of light. Using a triangular waveform, in contrast to a sawtooth waveform, allows both spatial and velocity information to be obtained as the object movement imparts a doppler shift to the echo signal frequency. The result is that the rising and falling portions of the waveform generate different beat frequencies which causes the peaks in the stationary frequency spectrum to be split by the doppler frequency $\delta f_D = 2f_0\cdot(\Delta v/c)$.

For the signal generation in a LiDAR system, indium phosphide (InP) provides mature PIC components and ability for active-passive integration to form an integrated transceiver [2,5,18-22]. This paper discusses the design and characterization of one such InP PIC transceiver which consists of a sampled grating distributed Bragg reflector (SGDBR) laser, a frequency discriminator based on an asymmetric Mach-Zehnder Interferometer (a-MZI) and balanced photodiodes (PD), and a receiver consisting of balanced PDs and couplers to mix the reference and echo signal. The paper is structured to first describe the components

Manuscript received February 1, 2019. This work was supported in part by DARPA AFOSR contract HR0011-16-C-0106 through a subcontract from Lockheed Martin. B. J. Isaac was supported by an NSF GRFP.

B. J. Isaac and L. A. Coldren are with the Materials Department, University of California, Santa Barbara, CA 93106 USA (email: brandonjisaac@ucsb.edu; coldren@ece.ucsb.edu).

B. Song, S. Pinna, and J. Klamkin are with Department of Electrical and Computer Engineering, University of California, Santa Barbara, CA 93106 USA. (e-mail: bowen@ece.ucsb.edu; pinna@ece.ucsb.edu; klamkin@ece.ucsb.edu)

This article has been accepted for publication in a future issue of this journal, but has not been fully edited. Content may change prior to final publication. Citation information: DOI 10.1109/JSTQE.2019.2911420, IEEE Journal of Selected Topics in Quantum Electronics

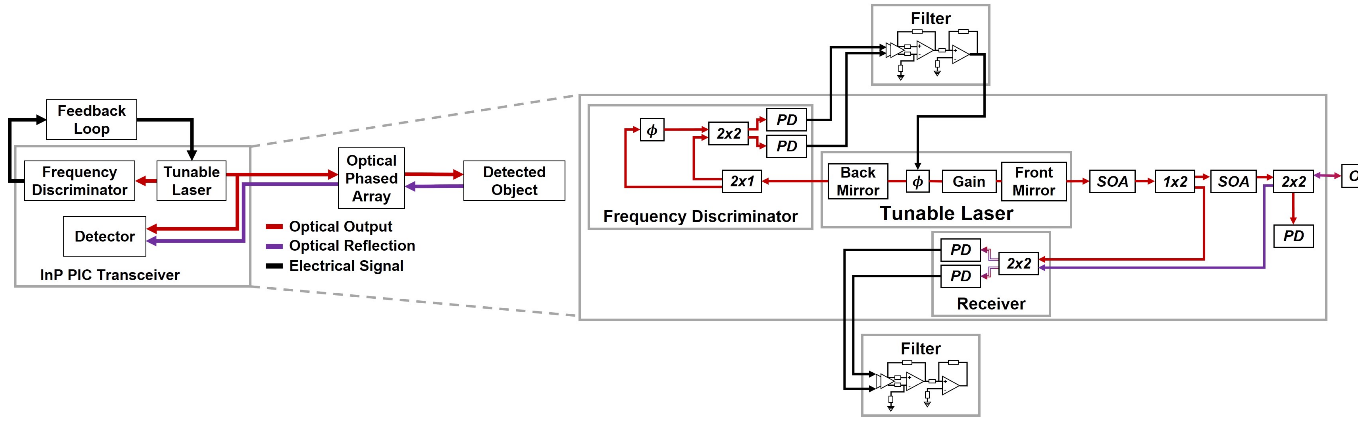

Fig. 1 Block diagram of the tranceiver and OPA system (left). The tunable laser provides a signal for the OPA and on-chip frequency discriminiator that drives an off-chip feedback circuit for frequency locking the laser. The detector utilizes tapped power from the tunable laser in a self-heterodyne measurement to convert object distance to a beat frequency as the tunable laser is frequency modulated. The expanded region (right) shows the tranceiver PIC components including gain, phase, and mirrors of the laser; semiconductor optical amplifier (SOA); 1x2 and 2x2 splitters; phase shifters; and photodetectors (PD).

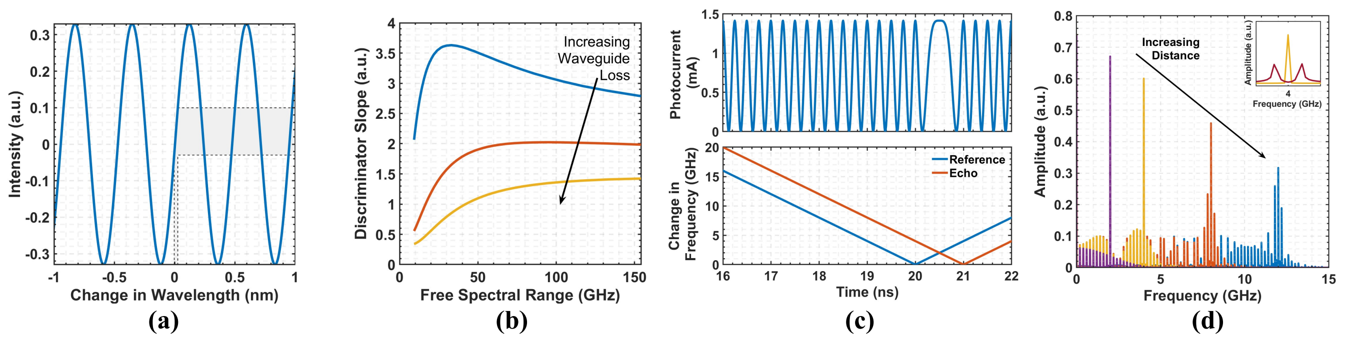

Fig. 2 (a) Output of a-MZI under balanced detection calculated from Eq. 1. The shaded region illustrates the amplitude change due to frequency changes of the laser output. (b) a-MZI based frequency discriminator sensitivity as the FSR varies for different passive waveguide losses. The orange curve uses a loss of 4 cm^{-1} typical for deep ridge waveguides in InP [23,24,26]. (c) Receiver operation principle. Bottom graph shows the instantaneous frequency of the reference and echo signal as a function of time. The top graph shows the measured photocurrent as the reference and echo signals beat together on the receiver PDs. (d) Frequency spectrum of the receiver photocurrent for reflections at different distances. The inset shows peak splitting due to the doppler effect for moving objects.

of the PIC transmitter with details to elucidate design choices and tradeoffs that were considered, followed by a discussion of the fabrication and characterization of transceiver components

II. PIC Overview and Component Theory

A block diagram of the LiDAR system is shown in Fig. 1, along with a more detailed block diagram of the InP transceiver. The InP transceiver PIC can be coupled to an OPA which serves as the emitting and receiving aperture. The transmitter and receiver are discussed in further details below.

A. Transmitter

The transmitter consists of a widely tunable laser and a frequency discriminator [18,23,24]. The tunable laser is an SGDBR laser which consists of a DBR laser modified by periodic blanking of the front and back grating mirrors at different sampling periods. This produces a Vernier-like reflection spectra allowing for wide tunability [25]. The SGDBR laser was designed for tuning over the wavelength range of 1530 nm to 1570 nm. Coarse tuning of the wavelength is achieved by differential injection of current into the front and back mirrors of the laser. Fine tuning is achieved by equal current injection into the mirrors, or by current injection in a phase shifter inside the SGDBR cavity which controls the cavity mode locations. The grating design of the SGDBR also considers the front-to-back splitting to obtain the desired LiDAR output power and the sensitivity of the frequency discriminator. For this purpose, the mirror reflections were designed to give a front-to-back power splitting ratio of 7:1 by optimizing the number of sampled grating bursts. Power from the front mirror is guided to two semiconductor optical amplifiers (SOA), and 1x2 and 2x2 splitters for the OPA and receiver. The two SOAs use the same gain material as the SGDBR laser but are tapered to increase the mode size to prevent gain saturation. The 1x2 splitter is utilized to tap power for use in the receiver as a reference to the echo signal. A second, 2x2, splitter is utilized for two purposes: first, to couple the reflected signal to the receiver, and second to measure chip temperature through an on-chip PD. The laser, SOAs, couplers, and PDs were all implemented in surface ridge waveguides to minimize passive waveguide loss.

Frequency stabilization is achieved using a tunable a-MZI filter using deep ridge waveguides. The a-MZI converts frequency fluctuations of the laser to amplitude fluctuations of the PD currents. Power from the back mirror of the SGDBR laser is split by a 1x2 multimode interference coupler (MMI)

This article has been accepted for publication in a future issue of this journal, but has not been fully edited. Content may change prior to final publication. Citation information: DOI 10.1109/JSTQE.2019.2911420, IEEE Journal of Selected Topics in Quantum Electronics

between the two different paths of the a-MZI. The longer path also contains a phase shifter for tuning the filter quadrature frequency. A 2x2 MMI mixes the output from the two paths to allow balanced photodetection, eliminating common mode noise from the SGDBR laser. The transfer matrix relating the input electric field amplitude to the photocurrents in each PD is shown below:

$$\begin{pmatrix} I_1 \\ I_2 \end{pmatrix} \propto \left| \begin{pmatrix} 1 & j \\ j & 1 \end{pmatrix} \begin{pmatrix} e^{(j\beta-\alpha)L_1} & 0 \\ 0 & e^{\phi} e^{(j\beta-\alpha)(L_1+\delta L)} \end{pmatrix} \begin{pmatrix} 1 & j \\ j & 1 \end{pmatrix} \begin{pmatrix} E_0 \\ 0 \end{pmatrix} \right|^2 \quad \text{Eq. (1)}$$

Here, E_0 is the square root of the laser output power, β is the propagation constant of the waveguide mode, α is the waveguide loss, L_1 is the length of the shorter path in the a-MZI, δL is the additional path length of the second path, ϕ is the tunable phase shift in the second path, and $I_{1,2}$ is photocurrent in each PD. The transfer function using balanced photodetection is shown in Fig. 2a. Equation 1 can be used to determine the sensitivity to frequency fluctuations by calculating $dI/d\lambda$ and taking the maximum value. The sensitivity of the discriminator is determined by the input optical power, waveguide loss, and the free spectral range (FSR) of the a-MZI which is given by $c\cdot(n_{eff}\Delta L)^{-1}$. The sensitivity is quantified in terms of the discriminator slope as shown in Fig. 2b. The sensitivity, or slope, increases as the FSR decreases; however, the additional path length required to reduce the FSR increases the total loss. This reduces the sensitivity, as the photocurrent amplitude is proportional to the square of the electric field amplitude at the input. To address this trade-off, an FSR of 60 GHz was selected based on previous loss values of 4 cm^{-1} reported for deep ridge waveguides in InP [23,24,26]. The photocurrents generated in each PD are input to an off-chip circuit containing a two-stage differential amplifier with an inverting input to create the balanced detection, and a two-stage op-amp filter to drive the difference in PD photocurrents to zero. The amplifiers and filter act to convert the error to a current and inject it into the phase section of the laser cavity. This tunes the frequency of the laser to the quadrature point of the a-MZI where the power is equally split between the two photodiodes and the error is zero.

The a-MZI also contains a phase shifter in one path to shift the output interference independent of the frequency of the laser. This control is referred to as the "chirp" to reduce confusion with phase shifter in the SGDBR cavity. Injecting current into the chirp section tunes the quadrature frequency where the a-MZI equally splits the power between the two PDs. When the laser is frequency locked by the external circuit, tuning the quadrature frequency allows control over the laser frequency. By applying a modulated current to the chirp, the PIC can be used to realize FMCW LiDAR.

B. Receiver

The receiver consists of a 2x2 splitter and two PDs, which act to self-heterodyne the laser output with the received echo. Utilizing a 2x2 splitter allows for balanced photodetection in the receiver circuit to reject common mode noise and signal. The echo signal is coupled back into the transceiver PIC through the same port that coupled the output into the OPA. As shown in Fig. 2c, the reference and echo signal differ in frequency due to the additional travel time of the echo signal. The bottom graph shows the instantaneous frequency of the reference and echo signal at the receiver. The top graph shows the current measured by the receiver PDs that contains the beat frequency of the two signals. Fig. 2d shows the calculated frequency spectrum of the PD current for measurements on objects at different distances to illustrate the change in the peak frequency of the photocurrent. The inset shows the peak splitting imparted by a moving object due to doppler frequency shifts as discussed previously. Also visible in the spectrums of Fig. 2d are satellite peaks arising from the beat frequency transient as the modulation changes direction (seen around 20 ns in Fig. 2c). This transient region sets the maximum range of the FMCW LiDAR system barring laser coherence length considerations. As the objects distance approaches one-half of the chirp period, the receiver photocurrent undergoes a constant frequency modulation and the spectrum is not peaked around a single value. Additionally, due to finite laser linewidth, there is a minimum detectable frequency shift, which affects the distance resolution as there will be some broadening in the frequency spectrum. The modulation period and rate must be selected to address desired range which is ultimately limited by the laser linewidth and frequency modulation bandwidth. The frequency locking technique described previously has demonstrated a linewidth of 570 kHz, which gives a maximum range of 160 m [24].

An important note on integration of the transmit and receive circuits for FMCW LiDAR, is the impact of the echo signal on the stability of the tunable laser. This can be broken down into three regimes: short-range (on-chip), medium-range, and long-range reflections. For the first case, all on-chip optical interfaces are angled to minimize reflections. Furthermore, it is well established that laser stability is not strongly influenced for very short external cavities [30,31]. In the case of medium-range reflections, where the reflected power may be significant, the frequency modulation detunes the instantaneous emitting frequency from the reflection such that the influence of the reflections is strongly reduced [32]. For long range reflections, in addition to frequency detuning, the power will be below the limit to influence stability.

III. Fabrication and Component Characterization

A. PIC Fabrication

An overview of the fabrication process is shown in Fig. 3a. The starting material for the transceiver PIC is grown by metal organic chemical vapor deposition (MOCVD) up to an InP cap above the quantum well (QW) "active" layers. The QWs are selectively removed from the "passive" regions outside of the SGDBR gain section, the SOA and the PDs using a wet chemical etch. The SGDBR sampled gratings are patterned using electron beam lithography and formed with a reactive-ion-etch (RIE). Next, the InP waveguide cladding and InGaAs p-contact are regrown using MOCVD. The waveguides are then defined using a combination of wet and dry chemical

This article has been accepted for publication in a future issue of this journal, but has not been fully edited. Content may change prior to final publication. Citation information: DOI 10.1109/JSTQE.2019.2911420, IEEE Journal of Selected Topics in Quantum Electronics

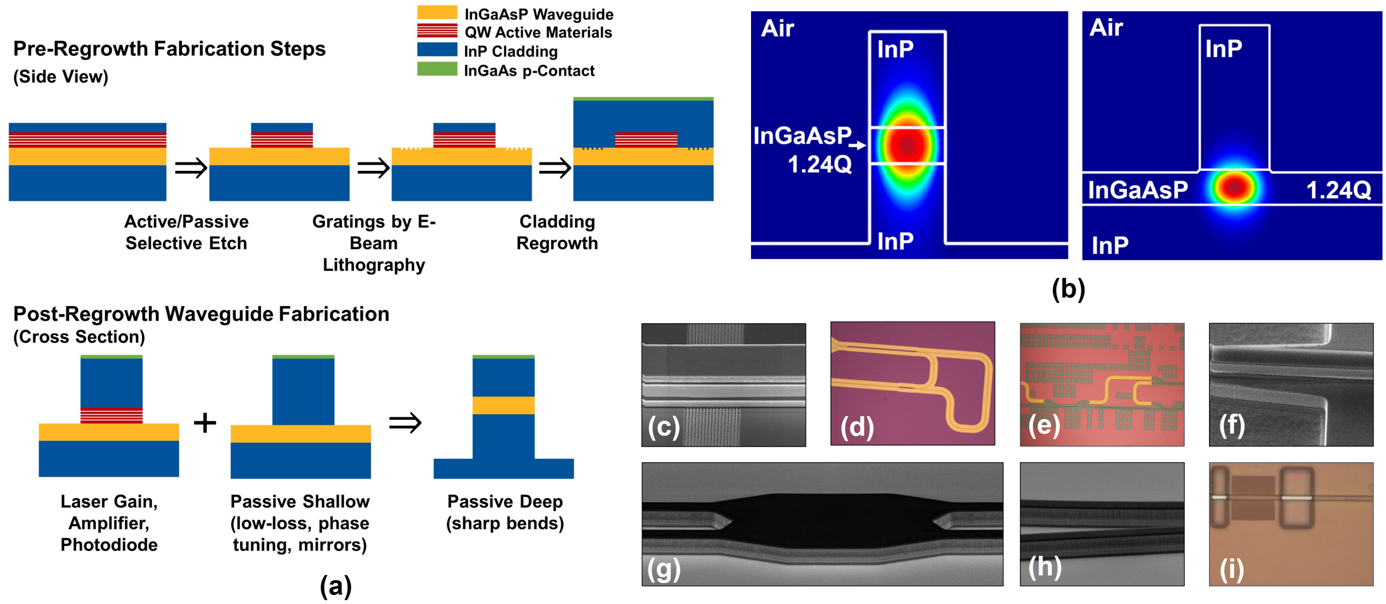

Fig. 3. (a) Overview of fabrication process for InP transceiver. The initial epitaxy structure is pattern to define the active regions with offset quantum wells. The gratings for the SGDBR laser are patterned and p-type InP and InGaAs are regrown by MOCVD for the cladding layer and p-contact. The waveguides are defined by wet and dry chemical etches to form the surface ridge waveguides for the laser, amplifiers, and photodiodes, and deep ridge waveguides for the sharp waveguide bends. (b) Optical mode simulations of the surface ridge and deep ridge waveguide structures used. (c-i) Images from fabrication showing various PIC components and processing steps. In order, these are the sampled gratings, a-MZI, waveguide definition, deep-to-shallow waveguide transition, 2x2 MMI, directional coupler and device isolation.

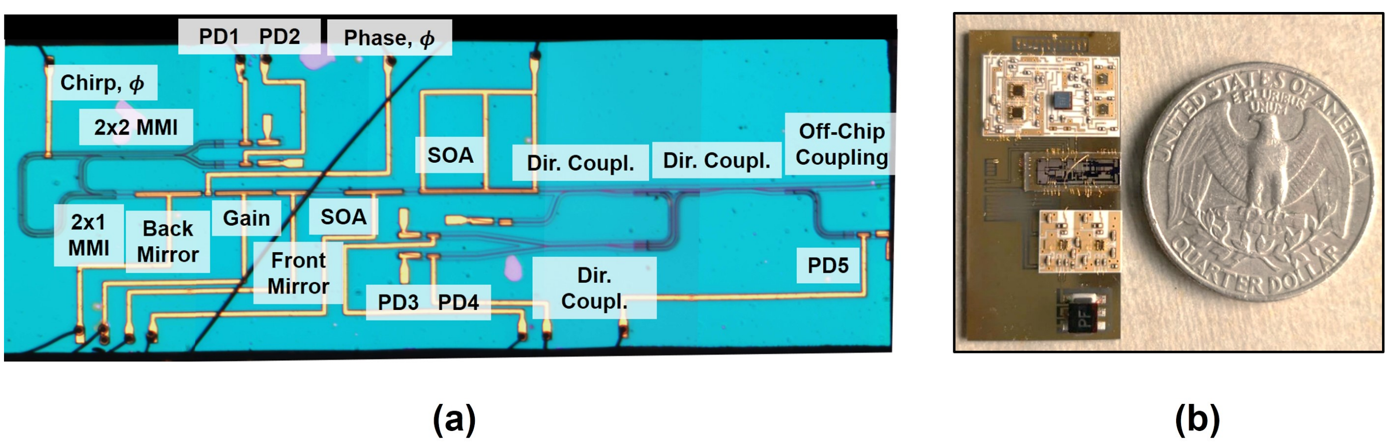

Fig. 4 (a) Image of fabricated PIC with components labeled. The dimensions are 8 mm x 2 mm. (b) Module for characterization of the PIC transceiver. The PIC is mounted on a carrier and sub-carrier which contains the electronics for the feedback circuit and receiver signal processing. The quarter is shown for scale.

etches to form both surface ridge and deep ridge waveguides [27-29]. Fig. 3b shows the simulation of optical modes for the two different types of waveguides. The deep ridge waveguide provides higher optical confinement, allowing for sharper bend radii to keep the PIC footprint relatively small, however, this adds additional passive loss due to mode overlap with the etched side wall which contain some roughness from the etch. The surface ridge waveguide uses a selective wet etch which stops on the waveguide layer and eliminates the loss due to sidewall roughness. Isolation between contacts of the electrodes is formed by removing the low resistance p-InGaAs layer on the top of the ridge waveguides, and a Ti/Pt/Au metal stack is deposited for the p-type contacts and probe pads. Figure 3c-i shows images of taken during fabrication showing the various components. The wafer is thinned, and backside metal is deposited for a common N-contact. Lastly, the wafer is cleaved to separate the individual PICs. Fig. 4a shows the final fabricated PIC. The PICs were mounted on carriers for integration with electronic lockers and receiver circuits as shown in Fig. 4b. Testing of the PICs consisted of the following: Current-Voltage measurements on the all diodes, Light-Current-Voltage (LIV) measurements of gain section using reverse biased SOA and PDs to measure optical power, SGDBR spectrum mapping using the front and back mirrors, LI measurements of the discriminator PDs as the phase and chirp sections are tuned, and frequency chirp control.

B. SGDBR Laser Performance

The measured LIV of the SGDBR laser is shown in Fig. 5a. The threshold current is around 45 mA with the laser output achieving 15 mW at 100 mA. Fig. 5b shows wavelength tuning

This article has been accepted for publication in a future issue of this journal, but has not been fully edited. Content may change prior to final publication. Citation information: DOI 10.1109/JSTQE.2019.2911420, IEEE Journal of Selected Topics in Quantum Electronics

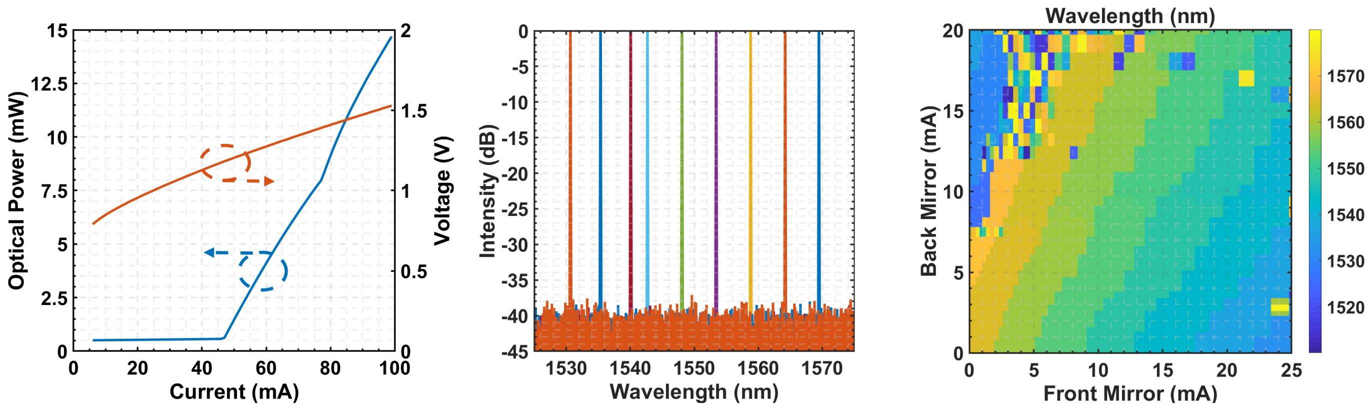

(a) (b) (c)

Fig. 5 (a) Light-current-voltage (LIV) measurement of the SGDBR laser. The laser threshold current is around 45 mA and an output power of 15 mW is achieved around 100 mA. The power is measured by reverse biasing the on-chip SOA. (b) Lasing spectrum over the tuning range of 1530 nm to 1570 nm. The side mode suppression ratio is greater than 37 dB for this range. (c) Wavelength tuning map as a function of current injection into the front and back mirror.

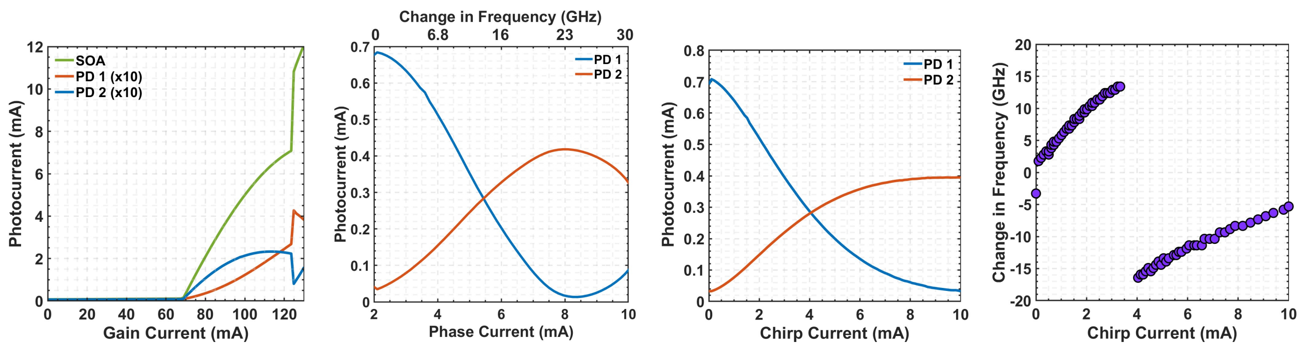

(a) (b) (c) (d)

Fig. 6 (a) Photocurrent measured by the SOA and two PDs of the frequency discriminator. The discontinuity around 120 mA is a result of a mode hop. (b) Photocurrent in each PD of the frequency discriminator as a function of the current injected into the phase section of the SGDBR cavity. The top axis shows the corresponding frequency change of the laser output measured using an optical spectrum analyzer. (c) Photocurrent in each PD of the frequency discriminator as a function of the current injected into the chirp section of the a-MZI. (d) The locking frequency offset as a function chirp current. This is obtained by taking multiple measurements at various a-MZI chirp and SGDBR phase currents and measuring the frequency of photocurrent crossing point.

from 1530 nm to 1570 nm with side mode suppression ratio greater than 37 dB over the entire tuning range. Fig. 5c shows a full tuning map as the current is varied in the front and back mirrors. In practice, this provides a look-up table to tune the laser frequency and sample a discrete set of angular point using an OPA. The output during the transient stabilization can be suppressed by reducing the gain of the on-chip SOAs. Additionally, identical SGDBR lasers have been characterized by our group showing free-running linewidths of 6 MHz [22]

C. Frequency Discriminator Response

Characterization of the frequency discriminator consists of first determining the power reaching the PDs, then tuning the lasing wavelength by using the phase shifter in the SGDBR cavity, followed by tuning of the filter spectral location using the chirp section in the a-MZI. The photocurrent detected by the discriminator PDs was measured alongside the SOA photocurrent as shown in Fig. 6a. The SOA measures the power from the front mirror, while the two discriminator PDs measure the power from the back mirror. As mentioned above, a front to back splitting ratio of 7:1 was expected from the front and back mirror designs. However, lower power was detected at the discriminator PDs, which we attribute to passive optical loss in the deep ridge waveguide of the a-MZI. The photocurrent in each detector as a function of phase current is shown in Fig. 6b. Current injection into the phase section of the SGDBR provides fine tuning of the laser frequency, which is measured on an Optical Spectrum Analyzer and shown on the top x-axis of Fig. 6b. As discussed in Section II, the a-MZI was designed to have an FSR of 60 GHz. Fig. 6b shows that the filter passes through half of a cycle in 30 GHz of frequency tuning. Lastly, the filter quadrature location is tuned using the chirp section in the a-MZI as shown in Fig. 6c.

The external locking circuits operates by injecting current into the phase section of the SGDBR such that the lasing frequency is located at the quadrature point of the a-MZI and equal power is distributed to the two PDs. By tuning the current injected into the chirp section, the quadrature frequency is changed, and the output of the feedback circuit changes to maintain the locking condition. Fig. 6d shows the offset lasing frequency tuning over 30 GHz as the chirp phase shifter current is tuned between 0 mA to 10 mA. By imparting a triangular waveform with a current modulation range of 10 mA, the frequency of the laser can be modulated continuously over 30 GHz with a tuning efficiency of 3 GHz/mA.

This article has been accepted for publication in a future issue of this journal, but has not been fully edited. Content may change prior to final publication. Citation information: DOI 10.1109/JSTQE.2019.2911420, IEEE Journal of Selected Topics in Quantum Electronics

D. Receiver

The receiver consists of two PDs and a 2x2 MMI. One input consists of the reference signal from the SGDBR laser and the second is the echo signal. Fig. 7 shows the measured photocurrent in each PD as the phase section of the SGDBR laser is tuned with no intentional reflection. With an intentional reflection present, this would undergo a similar beating response as seen in Fig 6b. As shown in Fig. 7, the reference signal provides greater than 1 mW of input power into the receiver. This falls into the regime of shot noise limited operation making the minimum detectable echo signal power around 1 nW [33].

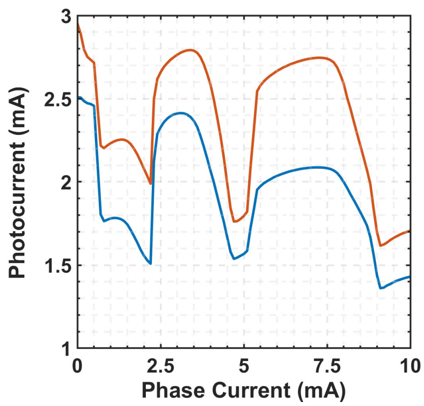

Fig. 7 Receiver photocurrent as a function of the SGDBR phase current. The large variations in the photocurrent are due to mode hops of the laser.

IV. Conclusion

We presented a PIC transceiver consisting of an SGDBR laser with an on-chip frequency discriminator for frequency locking and modulation for LiDAR applications. The components of the PIC were characterized to demonstrate functionality and the operating principles of the transceiver. Future experiments will implement one-dimensional ranging measurements. This can be achieved by imparting frequency modulation in the a-MZI and coupling to fiber with delay lines and 2x2 couplers to act as near perfect reflectors to extract the beat frequency at various delay lengths. In addition, the PIC transceiver can be butt-coupled to an OPA for full 2D beam-steering experiments and free space ranging measurements.

Acknowledgment

The authors acknowledge Paul Suni, James Colosimo, and S. J. Ben Yoo for technical discussions.

References

[1] L. A. Coldren, "Monolithic Tunable Diode Lasers," *IEEE Journal on Selected Topics in Quantum Electronics,* vol. 6, no. 6, 2000.

[2] S. Arafin and L. A. Coldren, "Advanced InP Photonic Integrated Circuit for Communication and Sensing," IEEE Journal of Selected Topics in Quantum Electronics, vol. 24, no. 1, January/February 2018.

[3] D. F. Welch, F. A. Kish, R. Nagarajan, C. H. Joyner, R. P. Schneider, V. G. Dominic, M. L. Mitchell, S. G. Grubb, T.-K. Chiang, D. D. Perkins and A. C. Nilsson, "The Realization of Large-Scale Photonic Integrated Circuits and the Associated Impact on Fiber-Optic Communication Systems," Journal of Lightwave Technology, vol. 24, no. 12, December 2006.

[4] R. Soref, "The Past, Present, and Future of Silicon Photonics," IEEE Journal of Selected Topics in Quantum Electronics, vol. 12, no. 6, November/December 2006.

[5] J. Klamkin, H. Zhao, B. Song, Y. Liu, B. Isaac, S. Pinna, F. Sang and L. Coldren, "Indium Phosphide Photonic Integrated Circuits: Technology and Applications," in IEEE BiCMOS and Compound Semiconductor Integrated Circuits and Technology Symposium, San Diego, CA, 2018.

[6] R. Nagarajan, M. Filer, Y. Fu, M. Kato, T. Rope and J. Stewart, "Silicon Photonics-Based 100 Gbit/s," Journal of Optical Communications and Networking, vol. 10, no. 7, 2018.

[7] T. Pinguet, S. Denton, S. Gloeckner, M. Mack, G. Masini, A. Mekis, Pang, Simon, M. Peterson, S. Sahni and P. De Dobbleaere, "High-Volume Manufacturing Platform for Silicon Photonics," Proceedings of the IEEE, vol. 106, no. 12, 2018.

[8] M.-C. Amann, T. B. M. Lescure, R. Myllyla and M. Rioux, "Laser Ranging: A Critical Review of Usual Techniques for Distance Measurement," Optical Engineering, vol. 40, no. 1, January 2001.

[9] M. Flood, "Laser Altimetry: From Science to Commercial LiDAR Mapping," Photogrammetric Engineering & Remote Sensing, November 2001.

[10] B. Schwarz, "Mapping the World in 3D," Nature Photonics Industry Perspective Technology Focus, vol. 4, 2010.

[11] H. K. Tsang, R. V. Penty, I. H. White, R. S. Grant, W. Sibbett, J. B. D. Soole, H. P. LeBlanc, N. C. Andreadakis, R. Bhat and a. M. A. Koza, "Two-photon absorption and self-phase modulation in InGaAsP/InP multi-quantum-well waveguides," Journal of Applied Physics, vol. 70, no. 3992, 1991.

[12] H. K. Tsang, C. S. Wong, T. K. Liang, I. E. Day, S. W. Roberts, A. Harpin, J. Drake and a. M. Asghari, "Optical dispersion, two-photon absorption and self-phase modulation in silicon waveguides at 1.5 µm wavelength," Applied Physics Letters, vol. 80, no. 416, 2002.

[13] L. Y. a. G. P. Agrawal, "Impact of two-photon absorption on self-phase modulation in silicon waveguides," Optics Letters, vol. 32, no. 14, 2007.

[14] C. C. L. a. H. Y. Fan, "Two-Photon Absorption and Photoconductivity in GaAs and InP," Applied Physics Letters, vol. 20, no. 18, 1972.

[15] S. Pinna, B. Song, L. A. Coldren and J. Klamkin, "Vernier Transceiver Architecture for Side-Lobe-Free and High-Etendue LiDAR," in Conference on Lasers and Electro-Optics, OSA Technical Digest (online), San Jose, CA, 2018.

[16] J. K. Doylend, M. J. R. Heck, J. D. Peters, M. L. Davenport, J. T. Bovington, L. A. Coldren, J. E. Bowers and J. C. Hulme, "Fully integrated hybrid silicon two-dimensional beam scanner," Optics Express, vol. 23, no. 5, 2005.

[17] J. K. Doylend, M. J. R. Heck, J. T. Bovington, J. D. Peters, L. A. Coldren and J. E. Bowers, "Two-dimensional free-space beam steering with an optical phased array on silicon-on-insulator," Optics Express, vol. 19, no. 22, 2011.

[18] B. Isaac, B. Song, S. Pinna, S. Arafin, L. Coldren and J. Klamkin, "Indium Phosphide Photonic Integrated Circuit Transmitter with Integrated Linewidth Narrowing for Laser Communications and Sensing," in EEE International Semiconductor Laser Conference (ISLC), Santa Fe, NM, 2018.

[19] P. R. A. Binetti, L. Mingzi, E. J. Norberg, R. S. Guzzon, J. S. Parker, S. Abirami, A. Bhardwaj, L. A. Johansson, M. J. Rodwell and L. A. Coldren, "Indium Phosphide Photonic Integrated Circuits for Coherent Optical Links," IEEE Journal of Quantum Electronics, vol. 48, no. 2, 2012.

[20] Y. A. Akulova, G. A. Fish, P.-C. Koh, C. L. Schow, P. Kozodoy, A. P. Dahl, S. Nakagawa, M. C. Larson, M. P. Mack, T. A. Strand, C. W. Coldren, E. Hegblom, S. K. Penniman, T. Wipiejewski and a. Larry, "Widely tunable electroabsorption-modulated sampled-grating DBR laser transmitter," IEEE Journal OF Selected Topics in Quantum Electronics, vol. 8, no. 6, 2002.

[21] J. Raring, L. Johansson, E. Skogen, M. Sysak, H. Poulsen, S. DenBaars and L. Coldren, "Single-Chip 40Gb/s Widely-Tunable Transceivers with Integrated SG-DBR Laser, QW EAM, UTC Photodiode, and Low Confinement SOA," in 2006 IEEE 20th International Semiconductor Laser Conference, Kohala Coast, HI, 2006.

[22] H. Zhao, S. Pinna, B. Song, L. Megalini, S. T. Š. Brunelli, L. A. Coldren and J. Klamkin, "Indium Phosphide Photonic Integrated Circuits for Free Space Optical Links," IEEE Journal of Selected Topics in Quantum Electronics, vol. 24, no. 6, 2018.

[23] A. Sivananthan, H.-c. Park, M. Lu, J. S. Parker, E. Bloch, L. A. Johansson, M. J. Rodwell and L. A. Coldren, "Monolithic Linewidth Narrowing of a Tunable SG-DBR Laser," in Proceedings OFC (OSA, 2013), Paper OTh3I.3, 2013.
[24] A. Sivananthan, H.-c. Park, M. Lu, J. S. Parker, E. Bloch, L. A. Johansson, M. J. Rodwell and L. A. Coldren, "Integrated Linewidth Reduction of a Tunable SG-DBR Laser," in in Proceedings CLEO (OSA, 2013), CTu1L.
[25] V. Jayaraman, Z.-M. Chuang and L. A. Coldren, "Theory, Design, and Performance of Extended Tuning Range Semiconductor Lasers with Sampled Gratings," IEEE Journal of Quantum Electronics, vol. 29, no. 6, 1993.
[26] J. S. Parker, E. J. Norberg, R. S. Guzzon, S. C. Nicholes and a. L. A. Coldren, "High verticality InP/InGaAsP etching in inductively coupled plasma for photonic integrated circuits," Journal of Vacuum Science & Technology B, vol. 29, no. 011016, 2011.
[27] L. Coldren, K. Furuya, B. Miller and J. Rentschler, "Combined dry and wet etching techniques to form planar (011) facets in GaInAsP/InP double heterostructures," Electronics Letters, vol. 18, no. 5, 1982
[28] S. Uekusa, K. Oigawa and M. Tacano, "Preferential Etching of InP for Submicron Fabrication with HCl/H3PO4 Solution," Journal of the Electrochemical Society, vol. 132, no. 3, 1985.
[29] F. Karouta, B. Docter, E. Kok, E.-J. Geluk, J. Van der Tol and M. Smit, "High Aspect Ratio Etching and Application in InP-Based Photonic Integrated circuits," in Electrochemical Society Fall Meeting, Honalulu, HI, 2008.
[30] K. Petermann, Laser Diode Modulation and Noise, Kluwer Academic Publishers, 1988.
[31] L. A. Coldren, S. W. Corzine and M. L. Masanovic, Diode Lasers and Photonic Integrated Circuits, Hoboken: John Wiley & Sons, Inc., 2012.
[32] L. A. Johansson and L. A. Coldren, "Wavelength-Tunable Receiver Channel Selection and Filtering Using SG-DBR Laser Injection-Locking," in OFC/NFOEC Technical Digest, Anaheim, 2005.
[33] K. Kikuchi and S. Tsukamoto, "Evaluation of the Sensitivity of the Digital Coherent Receiver," Journal of Lightwave Technology, vol. 26, no. 13, 2008.

Brandon J. Isaac received a B.S. degree in Chemical Engineering and Physics in 2013 from the University of Kentucky, Lexington, KY. He is working towards a Ph.D. in Materials at the University of California Santa Barbara with a focus on opto-electronic devices and photonic integrated circuits. Prior to joining the Integrated Photonics Lab at UCSB, he worked on oxide heterostructure growth in the UCSB Molecular Beam Epitaxy Lab. He is a student member of OSA and recipient of NSF GRFP.

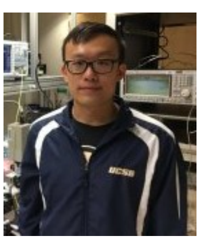

Bowen Song received the B.Eng. degree from the School of Electronic Engineering and Optoelectronic Technology, Nanjing University of Science and Technology, Nanjing, China, in 2012, and the M.Sc. degree from Boston University, Boston, MA, USA, in September 2014. He is currently working toward the Ph.D. degree at the Department of Electrical and Computer Engineering, UCSB, Santa Barbara, CA, USA. He is from Shanxi, China. In early 2013, he joined the Wide Bandgap Semiconductor Laboratory, Boston University, working on developing nano-patterned sapphire substrate for AlGaN-based deep UV LEDs. His current research interests include electronic-photonic integration, integrated photonics, and integrated Lidar

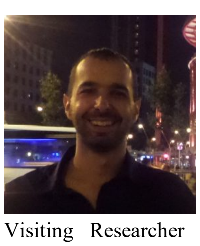

Sergio Pinna received the Ph.D. degree in innovative technologies from the Scuola Superiore Sant'Anna, Pisa, Italy, in 2014, and the B.Sc. and M.Sc. degrees in telecommunications engineering from the University of Pisa, Pisa, in 2008 and 2010, respectively. From November 2010 to December 2015, he was a Fellow with CNIT, National Photonic Networks Laboratory, Pisa. In 2014, he was a Visiting Researcher with the Integrated Photonics Laboratory, Boston University, Boston, USA. From January 2016, he was a Research Fellow with TeCIP Institute, Scuola Superiore Sant'Anna, Pisa, within the Digital and Microwave photonics group. In 2017, he joined the Integrated Photonics Laboratory, University of California Santa Barbara, as a Postdoctoral Research Associate. His research activity focuses on photonics for microwave applications and LiDAR sensors.

Larry A. Coldren is a Distinguished Professor Emeritus and Research Professor at the University of California, Santa Barbara, CA. He received his Ph.D. in EE from Stanford Univ. and spent 13 years in research at Bell Labs before joining UCSB in 1984. He has served as Director of several multi-university optoelectronics research centers, including one of the DARPA/Industry sponsored Optoelectronics Technology Centers throughout the 1990s. He also acted as Dean of Engineering at UCSB from 2009-2011. In 1991 he co-founded Optical Concepts, acquired as Gore Photonics, to develop novel Vertical-Cavity Surface-Emitting Laser (VCSEL) technology; and later in 1998, Agility Communications, acquired by JDS-Uniphase (now Lumentum), to develop widely-tunable integrated optical transmitters. At Bell Labs Coldren worked on Surface-Acoustic-Wave (SAW) filters and tunable coupled-cavity lasers using novel RIE technology that he was first to develop for the then new InP-based materials. At UCSB he continued work on multiple-section lasers, in 1988 inventing the widely-tunable multi-element mirror concept, now used in numerous commercial products. He has also made seminal contributions to efficient VCSEL designs, now used in high-speed data links. His group was first to suggest and demonstrate that gain elements should be placed only at E-field standing-wave maxima, which is key to all commercial VCSELs today. He continues efforts on high-performance InP-based photonic integrated circuits (PICs) and high-speed VCSELs. He has authored or co-authored over a thousand journal and conference papers, including numerous plenary, tutorial and invited presentations. He has also co-authored 8 book chapters and two textbooks, including the most used text on Diode Lasers and Photonic ICs in circulation today. Coldren has been issued 61 patents and is a recipient of several awards, including the John Tyndall, Aron Kressel, David Sarnoff, IPRM, and Nick Holonyak, Jr awards. He is a Life Fellow of the IEEE, and a Fellow of the OSA, the National Academy of Inventors, and IEE as well as a member of the National Academy of Engineering.

Jonathan Klamkin received the B.S. degree from Cornell University, Ithaca, NY, USA and the M.S. and Ph.D. degrees from the University of California Santa Barbara, Santa Barbara, CA, USA. From 2008 to 2011, he was a member of the Technical Staff in the Electro-Optical Materials and Devices Group, MIT Lincoln Laboratory, Lexington, MA, USA. From 2011 to 2013, he was an Assistant Professor at the Institute of Communication, Information and Perception Technologies at the Scuola Superiore Sant'Anna, Pisa, Italy. From 2013 to 2015, he was an Assistant Professor of Electrical and Computer Engineering (ECE) and Materials at Boston University, Boston, MA, USA. In 2015, he joined the ECE Department at the University of California Santa Barbara, where he is currently an Associate Professor and Director of the UCSB Nanotech. He is an Associate Editor for Photonics Technology Letters, Vice Chair for the Microwave Theory and Techniques Society Subcommittee on Microwave Photonics, and Steering Committee Member for the Journal of Lightwave Technology. He was Program Chair for the Integrated Photonics Research, Silicon and Nanophotonics Conference, in 2017, and General Chair for the same conference, in 2018. He or his group members received best paper awards at the 2006 Conference on Optoelectronic and Microelectronic Materials and Devices, the 2007 Microwave Photonics Conference, and the 2017 Asia Communications and Photonics Conference. He has published more than 180 journal and conference papers and holds three patents. He received the NASA Early Career Faculty Award and the DARPA Young Faculty Award. Prof. Klamkin is a senior member of the IEEE and OSA.